Probing the primordial Universe with MeerKAT and DES

José Fonseca,[1]★ Roy Maartens[1,2] and Mário G. Santos[1,3]

[1]*Department of Physics and Astronomy, University of the Western Cape, Cape Town 7535, South Africa*
[2]*Institute of Cosmology and Gravitation, University of Portsmouth, Portsmouth PO1 3FX, UK*
[3]*SKA SA, The Park, Park Road, Cape Town 7405, South Africa*

ABSTRACT

It is usually assumed that we will need to wait until next-generation surveys like *Euclid*, LSST and SKA, in order to improve on the current best constraints on primordial non-Gaussianity from the *Planck* experiment. We show that two contemporary surveys, with the SKA precursor MeerKAT and the Dark Energy Survey (DES), can be combined using the multitracer technique to deliver an accuracy on measurement of f_{NL} that is up to three times better than *Planck*.

Key words: cosmology: miscellaneous – large-scale structure of Universe.

1 INTRODUCTION

Future cosmological surveys will probe the three-dimensional large-scale structure of the Universe in ever larger volumes, delivering tighter and tighter constraints on cosmological parameters and modified gravity. Most of these surveys are based on sampling a large number of galaxies at optical or near-infrared wavelengths, such as *Euclid*[1] and LSST.[2] The SKA[3] will use the 21-cm emission of H I, both to detect H I galaxies and to map the integrated intensity from each pixel.

One of the key targets of these next-generation surveys is to go beyond the capability of cosmic microwave background (CMB) experiments in probing the primordial Universe – in particular to surpass CMB constraints on primordial non-Gaussianity. Primordial non-Guassianity in the fluctuations that are generated by inflation leaves a 'frozen' signal in the matter distribution on ultralarge scales, which is why ultralarge volume surveys will be able to improve on the CMB state of the art. In this paper, we only focus on local-type non-Gaussianity measured by the parameter f_{NL}. The current best bound on f_{NL} is from the *Planck* experiment, giving[4] $\sigma(f_{NL}) \simeq 6.5$ (Planck Collaboration XVII 2015).

Recent and current surveys, such as BOSS[5] and Dark Energy Survey (DES),[6] are unable to match the CMB accuracy on f_{NL}. Next-generation surveys are forecast to beat the *Planck* constraint (Alonso et al. 2015; Raccanelli et al. 2016). Even these surveys, using the galaxy power spectrum and a single tracer, will be unable to push $\sigma(f_{NL})$ below 1, which is needed to rule out some of the simplest inflationary models. The problem is cosmic variance, which

grows with the increase of scales being probed. A way to beat down cosmic variance is the multitracer technique, which combines the information from two or more surveys (or multiple tracers within the same survey; McDonald & Seljak 2009; Seljak 2009; Hamaus, Seljak & Desjacques 2011; Abramo & Leonard 2013). This technique is forecast to deliver game-changing improvements in $\sigma(f_{NL})$ from next-generation surveys (Yoo et al. 2012; Ferramacho et al. 2014; Yamauchi, Takahashi & Oguri 2014; Alonso & Ferreira 2015; Fonseca et al. 2015).

However, these improvements will only be available from future surveys in the coming decade. Hence, a question arises: Can surveys be combined within the next few years to match or improve CMB bounds on f_{NL}? We address this question, using the multitracer technique for two surveys. The multitracer confines us to use the overlap sky area and redshift range. Furthermore, the technique is more powerful the more different are the tracers of dark matter in each survey, and the more different are the systematics. This leads us to choose the two contemporary surveys: DES (optical/infrared telescope, photometry) and MeerKAT[7] (radio dish array, H I intensity mapping). Our forecast is that DES and MeerKAT combined can measure f_{NL} with *Planck*-level accuracy or better.

In Section 2, we review the large-scale effects of non-Gaussianity as well as the Fisher forecast method using the multitracer technique. Then we describe in Section 3 the experimental specifications for MeerKAT and DES. In Section 4, we present our results, and we conclude in Section 5.

2 THEORETICAL INGREDIENTS

2.1 Local primordial non-Gaussianity

Local primordial non-Gaussianity is described by a non-linear correction to the primordial Newtonian potential $\Phi(\boldsymbol{x})$:

$$\Phi = \phi + f_{NL}(\phi^2 - \langle\phi^2\rangle). \qquad (1)$$

★ E-mail: josecarlos.s.fonseca@gmail.com
[1] www.euclid-ec.org
[2] www.lsst.org
[3] www.skatelescope.org
[4] We use the large-scale structure convention, $f_{NL} = f_{NL}^{LSS} \simeq 1.3 f_{NL}^{CMB}$.
[5] www.sdss3.org/surveys/boss.php
[6] www.darkenergysurvey.org

[7] www.ska.ac.za/science-engineering/meerkat/

Here ϕ is a first-order Gaussian potential and the perturbed metric is $ds^2 = a^2[-(1+2\psi)d\eta^2 + (1-2\phi)dx^2]$. The galaxy power spectrum is altered by scale-dependent bias on large scales (Dalal et al. 2008; Matarrese & Verde 2008):

$$b(z, k) = b_{\rm L}(z) + 3 f_{\rm NL} \frac{[b_{\rm L}(z) - 1]\Omega_{\rm m} H_0^2 \delta_{\rm c}}{D(z)T(k)k^2}, \tag{2}$$

where $b_{\rm L}$ is the linear Gaussian bias, $\delta_{\rm c} \simeq 1.69$ is the critical matter density contrast for spherical collapse, T is the transfer function (normalized to 1 on large scales) and D is the growth factor (normalized to 1 at $z = 0$). On superequality scales, $T(k) \simeq 1$ and the bias grows as $f_{\rm NL} k^{-2}$. If we use the power spectrum to probe primordial non-Gaussianity, we therefore need to look at the largest scales possible. When using a single tracer of the dark matter distribution, the signal is eroded by cosmic variance, and even the next-generation ultralarge survey volumes are unable to achieve $\sigma(f_{\rm NL}) < 1$ (Alonso et al. 2015; Raccanelli et al. 2016). We deal with the cosmic variance problem by using multiple tracers, following the method of Fonseca et al. (2015).

2.2 Angular power spectrum with all relativistic effects

The observed number density or brightness temperature contrast is $\Delta^A(z, \boldsymbol{n})$, where $\boldsymbol{n}$ is the direction of observation and A labels the tracer. Its two-point correlators define the angular power spectra:

$$\left\langle \Delta^A(z, \boldsymbol{n})\Delta^B(z', \boldsymbol{n}') \right\rangle = \sum_\ell \frac{(2\ell+1)}{4\pi} C_\ell^{AB}(z, z') P_\ell(\boldsymbol{n}\cdot\boldsymbol{n}'), \tag{3}$$

where P_ℓ are the Legendre polynomials. The sky maps of the tracers are decomposed into spherical harmonic modes and the $a_{\ell m}$ are used as estimators. We assume that the $a_{\ell m}$ are Gaussian distributed. Since the universe has no preferred structure ($\langle a_{\ell m}\rangle = 0$), all the information will be encoded in the angular power spectra C_ℓ^{AB}, where $\langle a_{\ell m}^A a_{\ell' m'}^{B*}\rangle = \delta_{\ell\ell'}\delta_{mm'}C_\ell^{AB}$.

Extending the single-tracer case (Challinor & Lewis 2011) to multiple tracers, the angular power spectra across two redshift bins are given by

$$C_\ell^{AB}(z_i, z_j) = 4\pi \int d\ln k \, \Delta_\ell^{W_A}(z_i, k) \, \Delta_\ell^{W_B}(z_j, k) \, \mathcal{P}(k), \tag{4}$$

where z_i are the redshift bin centres and the dimensionless primordial curvature perturbation power spectrum is

$$\mathcal{P}(k) = A_{\rm s} \left(\frac{k}{k_0}\right)^{n_{\rm s}-1}. \tag{5}$$

Here the pivot scale is $k_0 = 0.05\,{\rm Mpc}^{-1}$, $A_{\rm s}$ is the amplitude and $n_{\rm s}$ is the spectral index. The theoretical transfer function $\Delta_\ell^A(z, k)$ [not to be confused with $T(k)$] defines the observable transfer function in each bin via the window function W:

$$\Delta_\ell^{W_A}(z_i, k) = \int dz \, p^A(z)W(z_i, z)\Delta_\ell^A(z, k). \tag{6}$$

Here p^A is a selection function for tracer A that is de facto the redshift distribution function of observed sources. For galaxy number counts, $p^A \propto dn^A/dz d\Omega$. For H I temperature intensity maps, $p^A \propto T^A$. The selection function accounts for the fact that we have different numbers of emitters at different redshifts. It therefore weights the relative importance of each redshift in the signal.

The observational window function centred on z_i is $W(z_i, z)$, and is the probability distribution function for a source to be inside the i-bin. This is broadly speaking a binning choice based on the experimental specifications. The window function can also be chosen

differently for different tracers, but when using the multitracer technique, it has to be the same. The product of the selection function and the window function is the tracer's effective redshift distribution function inside the bin, normalized so that $\int dz\, p^A(z)W(z_i, z) = 1$ for all z_i.

The observed fluctuations $\Delta^A(z, \boldsymbol{n})$, and thus the transfer functions $\Delta_\ell^A(z, k)$, are gauge independent and any gauge may be used to compute them. For galaxies, expressions have been given in Yoo (2010); Challinor & Lewis (2011); Bonvin & Durrer (2011) and for H I intensity mapping in Hall, Bonvin & Challinor (2013). In Newtonian gauge, we have (Di Dio et al. 2013; Fonseca et al. 2015)

$$\begin{aligned}
\Delta_\ell^A(k) &= \left[b^A \delta_k^{\rm s} + \left(b_e^A - 3 \right) \frac{\mathcal{H}v_k}{k} \right] j_\ell(k\chi) + \frac{kv_k}{\mathcal{H}} j_\ell''(k\chi) \\
&+ \frac{\ell(\ell+1)(2-5s^A)}{2} \int_0^\chi d\tilde{\chi} \frac{(\chi-\tilde{\chi})}{\chi\tilde{\chi}} \left(\tilde{\phi}_k + \tilde{\psi}_k \right) j_\ell(k\tilde{\chi}) \\
&+ \left(\frac{2-5s^A}{\mathcal{H}\chi} + 5s^A - b_e^A + \frac{\mathcal{H}'}{\mathcal{H}^2} \right) \Bigg[v_k j_\ell'(k\chi) + \psi_k j_\ell(k\chi) \\
&+ \int_0^\chi d\tilde{\chi} \left(\tilde{\phi}_k' + \tilde{\psi}_k' \right) j_\ell(k\tilde{\chi}) \Bigg] \\
&+ \frac{(2-5s^A)}{\chi} \int_0^\chi d\tilde{\chi} \left(\tilde{\phi}_k + \tilde{\psi}_k \right) j_\ell(k\tilde{\chi}) \\
&+ \left[\psi_k + \left(5s^A - 2 \right) \phi_k + \frac{\phi_k'}{\mathcal{H}} \right] j_\ell(k\chi),
\end{aligned} \tag{7}$$

where we have suppressed the redshift dependence, $\mathcal{H}$ is the conformal Hubble parameter, χ is the comoving line-of-sight distance and v_k is the peculiar velocity. For Λ cold dark matter (CDM) and standard dark energy models, the metric perturbations are equal: $\psi_k = \phi_k$.

The first term on the right-hand side of equation (7) is the contribution from the tracer fluctuations, where $\delta^{\rm s}$ is the dark matter density contrast in the matter rest frame, equivalently in synchronous gauge. It is necessary to use the rest frame in order to avoid gauge dependence in the definition of bias (Bonvin & Durrer 2011; Challinor & Lewis 2011; Bruni et al. 2012; Jeong, Schmidt & Hirata 2012). In the presence of non-Gaussianity, the bias $b^A(z, k)$ of tracer A is given by (2), with $b_{\rm L} \rightarrow b_{\rm L}^A$. The evolution bias, $b_e^A(z)$, accounts for the redshift evolution of the sources for tracer A:

$$b_e^A = -\frac{\partial \ln\left[(1+z)^{-3}N^A\right]}{\partial \ln(1+z)}, \tag{8}$$

where N^A is the background number density, of galaxies or H I atoms.

The second term on the right-hand side of equation (7) is the redshift-space distortion contribution, which is independent of the chosen tracer (given the assumption that there is no velocity bias).

The second line of equation (7) gives the contribution of lensing convergence to the tracer fluctuations, integrated along the line of sight to each source. The lensing effect is modified by the magnification bias, s^A. Here, we need to make a careful distinction between number counts and intensity mapping. At linear order, there is no lensing contribution to the H I intensity fluctuations. This follows from conservation of surface brightness in gravitational lensing, similar to the case of CMB temperature fluctuations. It turns out that the H I brightness temperature fluctuations coincide with the H I atom number density fluctuations, provided that we set $s^{\rm H I} = 2/5$, which removes the lensing contribution, and some other

terms in equation (7) related to the luminosity distance fluctuations (Hall et al. 2013). For galaxy number counts, s^G is the logarithmic slope of the cumulative luminosity function $N^A(z, m < m_*)$ at the magnitude limit m_* of the survey. Thus, we have

$$s^{\text{H\,\textsc{i}}} = \frac{2}{5}, \tag{9}$$

$$s^G = \frac{\partial \log_{10} N^G}{\partial m_*}. \tag{10}$$

In the third line of equation (7), there is a Doppler term and a Sachs–Wolfe term. The fourth and fifth lines are integrated Sachs–Wolfe and time delay terms, respectively, while the final line is a further Sachs–Wolfe type contribution. The last four lines of equation (7) are the horizon-scale relativistic effects, which have k-dependences of $(\mathcal{H}/k)\delta_k^{\text{s}}$ and $(\mathcal{H}/k)^2\delta_k^{\text{s}}$. This follows from the Euler equation, which gives $v_k = f(\mathcal{H}/k)\delta_k^{\text{s}}$, and the Poisson equation, which gives $\phi_k \propto (\mathcal{H}/k)^2\delta_k^{\text{s}}$. Note that the first line also contains a horizon-scale term, since $\mathcal{H}v_k/k = f(\mathcal{H}/k)^2\delta_k^{\text{s}}$.

These relativistic terms become relevant on the same ultralarge scales, where local primordial non-Gaussianity is boosting the power spectrum via the bias, (2). For accurate constraints on f_{NL}, we need to include the relativistic terms. In the single-tracer case, this has been done by Camera, Santos & Maartens (2015a), Alonso et al. (2015), Raccanelli et al. (2016). Note that the best-fitting value of f_{NL}, as opposed to the measurement error $\sigma(f_{\text{NL}})$, can be significantly biased if the relativistic terms are omitted (Camera, Maartens & Santos 2015b). For the multitracer case, the relativistic effects can be detected and simultaneously $\sigma(f_{\text{NL}}) < 1$ can be achieved, as shown by Yoo et al. (2012) when neglecting all integrated terms in equation (7), and by Alonso & Ferreira (2015); Fonseca et al. (2015) in the general case.

2.3 Fisher forecasts with multiple tracers

The Fisher matrix for a set of parameters $\{\vartheta_i\}$ is

$$F_{\vartheta_i\vartheta_j} = \frac{1}{2}\text{Tr}\left[\left(\partial_{\vartheta_i}C\right)\Gamma^{-1}\left(\partial_{\vartheta_j}C\right)\Gamma^{-1}\right], \quad \Gamma = C + \mathcal{N}, \tag{11}$$

where C is the covariance matrix of the estimator and $\mathcal{N}$ is the noise contaminant, which we assume is independent of f_{NL}. For instrumental noise in radio surveys this is necessarily true, but it may not hold for shot noise, since non-Gaussianity induces deviations in halo overdensity from the pure Poisson sampling noise case – see Hamaus et al. (2011) for a discussion. However, the same authors conclude that this correction is tiny if one considers a large halo mass bin, which will be the case in this paper, hence justifying our assumption. If the angular power spectrum $C_\ell^{AB}(z_i, z_j)$ is the estimator's covariance, then we need to account for all multipoles and equation (11) becomes (Tegmark, Taylor & Heavens 1997)

$$F_{\vartheta_i\vartheta_j} = \sum_{\ell_{\text{min}}}^{\ell_{\text{max}}} \frac{(2\ell + 1)}{2} f_{\text{sky}} \text{Tr}\left[\left(\partial_{\vartheta_i}C_\ell\right)\Gamma_\ell^{-1}\left(\partial_{\vartheta_j}C_\ell\right)\Gamma_\ell^{-1}\right], \tag{12}$$

where f_{sky} is the fraction of sky surveyed. The multitracer technique requires that we use the same sky maps of two (or more) differently biased tracers. Not only should the sky areas be the same, but also the binning in redshift, so that we are always comparing the same patch of the universe. If we use an H\,\textsc{i} intensity map survey and a galaxy survey, we can schematically represent the covariance matrix

as (Ferramacho et al. 2014)

$$C_\ell^{AB}(z_i, z_j) = \begin{pmatrix} C_{\ell,ij}^{\text{H\,\textsc{i}},\text{H\,\textsc{i}}} & C_{\ell,ij}^{\text{H\,\textsc{i}},\text{G}} \\ \\ C_{\ell,ij}^{\text{G},\text{H\,\textsc{i}}} & C_{\ell,ij}^{\text{G},\text{G}} \end{pmatrix}. \tag{13}$$

Note that if we have n bins then the covariance matrix is $2n \times 2n$ for two tracers. The autotracer correlations are symmetric, but not the cross-correlations. Nevertheless, the overall angular power is symmetric with $C_{\ell,ij}^{\text{H\,\textsc{i}},\text{G}} = C_{\ell,ji}^{\text{G},\text{H\,\textsc{i}}}$. We do not include foregrounds and systematics in the full covariance matrix Γ. Note that, in addition to the reduction of cosmic variance, the multitracer technique also lessens the individual systematics of the two experiments and reduces the impact of foreground residuals.

Assuming that for Gaussian likelihoods the inverse of the Fisher matrix approximates well the parameter covariance, the marginal error in a parameter is given by

$$\sigma_{\vartheta_i} = \left[(F^{-1})_{\vartheta_i\vartheta_i}\right]^{1/2}. \tag{14}$$

3 SURVEYS

The multitracer technique is more effective if the differences between the tracers, and between the experimental characteristics, are large. An intensity map in the radio and a photometric galaxy survey have very different experimental features and the bias, evolution bias and magnification bias are also very different. We combine the two premier contemporary surveys of these types – an H\,\textsc{i} intensity survey with MeerKAT and a galaxy survey with DES.

3.1 MeerKAT H\,\textsc{i} intensity map

MeerKAT will be composed of 64 antennas and will operate from 2017. A proposed cosmological survey MeerKLASS (Santos et al., in preparation) includes an H\,\textsc{i} intensity map survey. Forecasts for such a survey have been investigated (Bull 2016; Pourtsidou et al. 2016a; Pourtsidou, Bacon & Crittenden 2016b), showing that MeerKAT can provide very good cosmological constraints.

In H\,\textsc{i} intensity mapping, all galaxies with H\,\textsc{i} contribute to the signal. To compute the angular power spectrum, we use the transfer function multipoles given by equation (7) together with equation (9). For brightness temperature fluctuation maps, the selection function follows the H\,\textsc{i} temperature, $p^{\text{H\,\textsc{i}}}(z) \propto T^{\text{H\,\textsc{i}}}(z)$, which we fit using the results of Santos et al. (2015).

The Gaussian H\,\textsc{i} bias, $b_{\text{L}}^{\text{H\,\textsc{i}}}$, is modelled by weighting the halo bias with the H\,\textsc{i} content in the dark matter haloes, and is shown in Fig. 1: details of the modelling are given in Santos et al. (2015). In our forecasts, we marginalize over the H\,\textsc{i} and galaxy bias – we use the modelled bias only to set the fiducial bias value in each redshift bin.

Given the background relation between $N^{\text{H\,\textsc{i}}}$ and $T^{\text{H\,\textsc{i}}}$, the H\,\textsc{i} evolution bias equation (8) becomes (Hall et al. 2013)

$$b_e^{\text{H\,\textsc{i}}}(z) = -\frac{\partial\left[\ln T^{\text{H\,\textsc{i}}}(z)\mathcal{H}(z)(1 + z)^{-1}\right]}{\partial\ln(1 + z)}. \tag{15}$$

The noise angular power spectrum for an experiment with N_{d} collecting dishes, total observation time t_{tot} and observed sky area S_{area}, is given by

$$\mathcal{N}_{ij}^{\text{H\,\textsc{i}}} = \frac{S_{\text{area}}}{2N_{\text{d}}t_{\text{tot}}} \int d\nu\, T_{\text{sys}}^2(\nu)\, \bar{W}_\nu(\nu, \nu_i)\, \bar{W}_\nu(\nu, \nu_j), \tag{16}$$
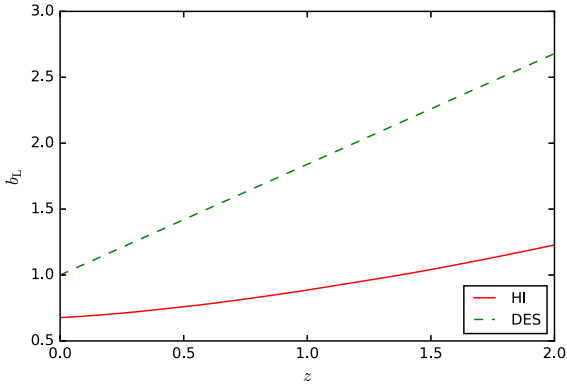
Figure 1. Gaussian bias for H I intensity (solid, red) and DES (dashed, green).
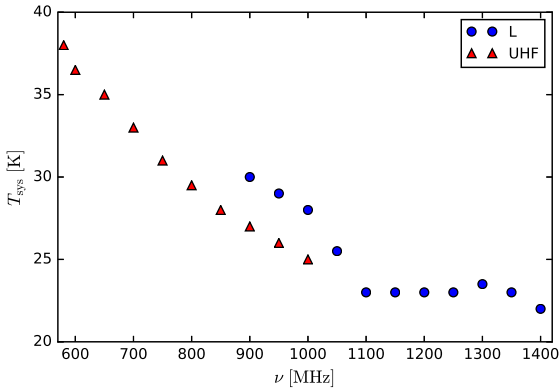

Figure 2. MeerKAT system temperature for *L* band (blue dots) and *UHF* band (red triangles).

where T_{sys} is the system temperature of the receiver. The window function in frequency is equivalent to the one in redshift, given that $\bar{W}_\nu(\nu, \nu_i) = \bar{W}(z, z_i) \, dz/d\nu$ and that the window is normalized: $\int d\nu \, \bar{W}_\nu(\nu, \nu_i) = 1$. The expression (16) is more general than what is commonly found in the literature and is valid when we do not consider a top hat window function. This allows us to deal correctly with the noise even when the bins overlap. In the case of a top-hat window function, we recover the conventional result (Santos et al. 2015), assuming a constant system temperature in the band.

There is also a shot-noise term in intensity mapping, since the signal requires the existence of galaxies in order to produce the emission lines. However, for H I, this shot-noise term is quite small and can be safely neglected (Gong et al. 2011).

MeerKAT's bands are

$$L: \quad 900 < \nu < 1670 \, \text{MHz}, \quad 0.58 > z > 0, \tag{17}$$

$$UHF: \quad 580 < \nu < 1015 \, \text{MHz}, \quad 1.45 > z > 0.40. \tag{18}$$

Although the total bandwidths are similar, the *UHF* band will probe a larger physical volume, allowing in principle for better cosmological measurements. Fig. 2 shows the system temperature for the MeerKAT bands.

3.2 DES photometric galaxy survey

DES is a 5000 deg^2 photometric galaxy survey in the southern sky, currently underway. In order to determine the observational details for forecasts, we followed closely the approach taken by

Alonso et al. (2015, their section 7.1) for a DES-like photometric galaxy survey.

Following Alonso et al. (2015), we adopt a simulation-based model (Weinberg et al. 2004) for the Gaussian galaxy bias (see Clerkin et al. 2015 for alternative bias models):

$$b_L^G = 1 + 0.84z. \tag{19}$$

Note that this bias model is used only to set the fiducial value in each redshift bin, since we marginalize over bias.

We use an r'-band Schechter luminosity function, as given by Gabasch et al. (2006). We approximate $r' \simeq r$ and use the following parametrization of the Schechter function:

$$\alpha = -1.33, \quad M_*(z) = -21.49 - 1.25 \ln(1 + z), \tag{20}$$

$$\varphi(z) = 2.59 - 0.136z - 0.081z^2 \quad [10^{-3} \, \text{Mpc}^{-3}]. \tag{21}$$

Here α is the slope of the low end of the luminosity function, and M_* is the magnitude of transition from lower to higher luminosities. The absolute magnitude M and apparent magnitude m are related by

$$M = m(z) - 25 - 5 \log_{10} \frac{d_L(z)}{\text{Mpc}} - k(z), \tag{22}$$

where d_L is the luminosity distance and the k-correction is taken as $k(z) \simeq 1.5z$ (Alonso et al. 2015).

We then use equations (20) and (21) in the Schechter luminosity function to estimate (with a five-point stencil numerical derivative) the magnification bias (10), which we fit with the polynomial

$$s^G(z) = 0.132 + 0.259z - 0.281z^2$$
$$+ 0.691z^3 - 0.409z^4 + 0.152z^5. \tag{23}$$

We truncated the polynomial once the error between the estimate and the fit to the polynomial was <1 per cent.

DES will observe galaxies with magnitude $r < 24$ and the redshift distribution of sources that we obtain is modelled as

$$\frac{dn^G}{dz} = 22.36 \left(\frac{z}{0.57}\right)^{1.04} \exp\left[-\left(\frac{z}{0.57}\right)^{1.34}\right] \text{arcmin}^{-2}. \tag{24}$$

The overall normalization agrees with DES science verification data (Bonnett et al. 2016). Using the relation between n^G and N^G, the evolution bias (8) is given by

$$b_e^G = -\frac{\partial \ln\left[(1+z)\mathcal{H}\chi^{-2} dn^G/dz\right]}{\partial \ln(1+z)}. \tag{25}$$

The noise angular power spectrum for a galaxy survey is dominated by shot noise (Alonso et al. 2015):

$$\mathcal{N}_{ij}^G = \frac{1}{N_i^G N_j^G} \int dz \frac{dn^G}{dz} W\left(z, z_i; \Delta z_i, \sigma_i^z\right) W\left(z, z_j; \Delta z_j, \sigma_j^z\right), \tag{26}$$

where N_i^G is the number of galaxies per steradian in the i-bin:

$$N_i^G = \int dz \frac{dn^G}{dz} W\left(z, z_i; \Delta z_i, \sigma_i^z\right). \tag{27}$$

W is the window function centred at z_i with bin size Δz_i and photometric redshift scatter $\sigma_i^z = \sigma_0(1 + z_i)$, with $\sigma_0 = 0.05$ for DES. For a photometric survey, the window function is given by a combination of error functions (Ma, Hu & Huterer 2005),

$$W\left(z, z_i; \Delta z_i, \sigma_i^z\right) = \frac{1}{2}\left[\text{erf}\left(\frac{z_i + \Delta z_i - z}{\sqrt{2}\,\sigma_i^z}\right)\right.$$

$$\left. - \text{erf}\left(\frac{z_i - \Delta z_i - z}{\sqrt{2}\,\sigma_i^z}\right)\right]. \qquad (28)$$

Equation (26) is also valid when different redshift bins overlap, which is the case we consider. Note that if we consider a top-hat window function, we recover the result commonly found in the literature $\mathcal{N}_{ii}^{\mathrm{G}} = 1/N_i^{\mathrm{G}}$.

3.3 H I–G cross-noise

We also take into account the possible shot-noise cross power spectrum. This is due to an overlap in the halo mass range that the tracers probe. Even if this is small, it might be important for the multitracer, since this is the only component in the noise matrix (30) corresponding to the cross-correlation between tracers. We are assuming Poisson noise. Simulations have shown that non-overlapping mass ranges can exhibit off-diagonal shot noise, and mass-dependent weighting schemes can suppress the total shot-noise contamination (Hamaus et al. 2010). However, the error in estimating the cross-correlation between tracers is dominated by the individual noises in each tracer, so that our Poisson assumption is not unreasonable. Then the cross-shot-noise is given by (Fonseca et al. 2015)

$$\mathcal{N}_{ij}^{\mathrm{H\,I,G}} = \int \mathrm{d}z\, \bar{W}\left(z, z_i; \Delta z_i, \sigma_i^z\right) W\left(z, z_j; \Delta z_j, \sigma_j^z\right) \frac{T^{\mathrm{H\,I}}(z)}{\rho_{\mathrm{H\,I}}(z)N_j^{\mathrm{G}}}$$

$$\times \int \mathrm{d}M_h\, M_{\mathrm{H\,I}}(M_h)\,\Theta\left(M_h, z\right) \frac{\mathrm{d}N_h}{\mathrm{d}M_h}(M_h, z) = \mathcal{N}_{ji}^{\mathrm{G,H\,I}}, \qquad (29)$$

where $\rho_{\mathrm{H\,I}}$ is the H I density, $M_{\mathrm{H\,I}}$ is the mass of H I in a halo of mass M_h, and $\mathrm{d}N_h/\mathrm{d}M_h$ is the halo mass function. If the halo masses probed by the two surveys overlap, then $\Theta(M_h) = 1$, otherwise it is zero. For further details on the halo mass range for H I intensity mapping, see Santos et al. (2015). The mass range for a photometric survey is found by matching the number of galaxies given by the halo mass function with the number given by the selection function. Note that the two windows have similar shapes but different normalizations, i.e. $\bar{W} \propto W$. While W is given by equation (28), $\bar{W}$ is the same as in equation (16) and is normalized to 1.

Including all noise contributions, we can write the multitracer noise angular power spectrum matrix as

$$\mathcal{N}_{ij}^{AB} = \begin{pmatrix} \mathcal{N}_{ij}^{\mathrm{H\,I}} & \mathcal{N}_{ij}^{\mathrm{H\,I,G}} \\ \\ \mathcal{N}_{ij}^{\mathrm{G,H\,I}} & \mathcal{N}_{ij}^{\mathrm{G}} \end{pmatrix}. \qquad (30)$$

Note that it is independent of the multipole ℓ.

4 RESULTS

We perform the Fisher forecast analysis as described in Section 2 for the set of parameters

$$\vartheta_\alpha = \{\ln A_s, \ln \Omega_{\mathrm{cdm}}, f_{\mathrm{NL}}, \ln n_s, \ln \Omega_{\mathrm{b}}, w, b_i^A, \varepsilon_{\mathrm{WL}}, \varepsilon_{\mathrm{GR}}\}, \qquad (31)$$

where Ω_{cdm} is the density parameter of CDM, Ω_{b} is the density parameter of baryonic matter and w is the dark energy equation of state parameter. We assume a fiducial concordance flat cosmology with $H_0 = 67.74\,\mathrm{km\,s^{-1}\,Mpc^{-1}}$, $\Omega_{\mathrm{cdm}} = 0.26$, $\Omega_{\mathrm{b}} = 0.05$, $A_s = 2.142 \times 10^{-9}$, $n_s = 0.967$, $w = -1$ and $f_{\mathrm{NL}} = 0$. The bias

parameters b_i^A in each bin have fiducial values shown in Fig. 1. The last two parameters in (31) have fiducial values $\varepsilon_{\mathrm{WL}} = 1 = \varepsilon_{\mathrm{GR}}$, and are defined so as to isolate the weak lensing and general relativistic terms in equation (7):

$$\Delta_\ell^A = \Delta_\ell^A(\text{density} + \text{RSD}) + \varepsilon_{\mathrm{WL}}\Delta_\ell^A(\text{WL}) + \varepsilon_{\mathrm{GR}}\Delta_\ell^A(\text{GR}). \qquad (32)$$

These parameters take into account that we do not have full knowledge of the evolution and magnification biases in (7).

To compute the multitracer angular power spectrum we modified the code CAMB_sources (Challinor & Lewis 2011) so that it computes both auto- and cross-tracer correlations with the correct selection function. We also changed it to compute the correct evolution bias of each tracer and to have different window functions as options. The output is in the same format as CAMB_sources. The modified code is available on GitHub.[8]

We computed forecasts for the single surveys and the combined surveys, with the following configurations:

MeerKAT *L* Band: 24 bins of width 20 MHz between 1380 and 920 MHz; sky coverage from 1000 to 30 000 deg^2; a smooth top-hat window function.

MeerKAT *UHF* Band: 21 bins of width 20 MHz between 1000 and 600 MHz; sky coverage from 1000 to 30 000 deg^2; a smooth top-hat window function.

DES: 8 bins in the redshift range $z = 0$–2, each with the same number of galaxies; sky coverage from 1000 to 5000 deg^2; an error window function.

Multitracer: *L* Band × DES: 4 bins that coincide with the first 4 bins taken for DES alone; sky overlap of 1000 to 5000 deg^2; an error window function.

Multitracer: *UHF* Band × DES: 5 bins between $z = 0.40$ and 1.45; sky overlap of 1000 to 5000 deg^2; an error window function.

The minimum ℓ used in our forecasts depends on the surveyed area: $\ell_{\min} = 1 +$ the integer part of $\pi/\sqrt{S_{\mathrm{area}}}$. For the maximum ℓ, we only consider information in the Fisher matrix if the scales are within the linear regime, as defined by (Smith et al. 2003)

$$k_{\mathrm{NL}}(z) = k_{\mathrm{NL},0}\,(1 + z)^{2/(2+n_s)}, \quad \text{with} \quad k_{\mathrm{NL},0} \simeq 0.2h\,\mathrm{Mpc^{-1}}. \qquad (33)$$

Using the Limber approximation, $\ell_{\max} \simeq \chi k_{\mathrm{NL}}$. Each redshift bin has its own corresponding $\ell_{\max,i}$. We therefore neglect the information coming from the *i*-th bin in the sum of the Fisher matrix (12) when $\ell > \ell_{\max,i}$. This will only be necessary for the low-redshift bins. For higher redshifts, we impose the global maximum $\ell_{\max} = 300$, since the additional information from higher ℓ (within the linear regime), provides very little improvement on the constraints.

The main results of this paper can be seen in Fig. 3 and Table 1, where we fix the MeerKAT observational time at 4000 h. The error on f_{NL} has been marginalized over the other parameters in equation (31). None of the surveys on their own can match the accuracy on f_{NL} of *Planck* (although DES is close). But with the multitracer technique, MeerKAT combined with DES over an overlap area of ∼4000–5000 deg^2, improves significantly on the *Planck* $\sigma(f_{\mathrm{NL}})$ – for both bands. (Note that the steps seen in the curves in Fig. 3 come from the fact that as the surveyed area decreases, the minimum accessible ℓ increases.)

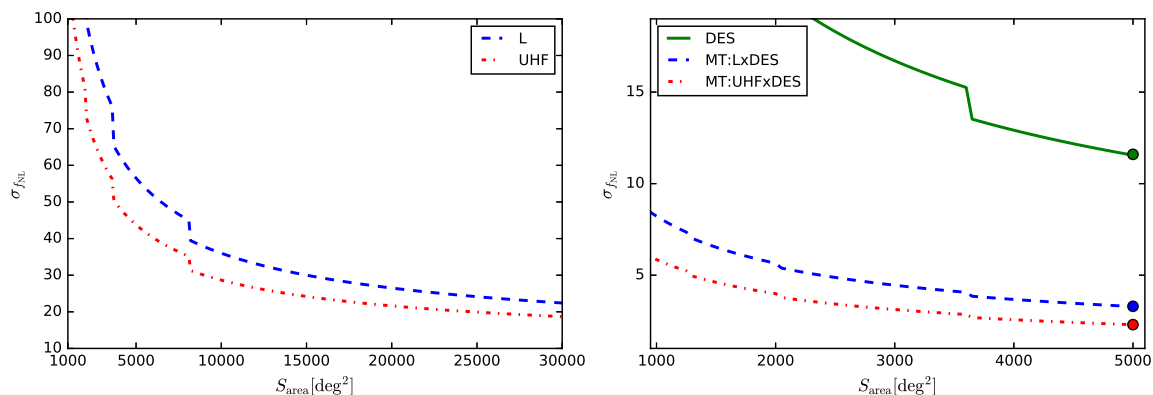---

[8] https://github.com/ZeFon/CAMB_sources_MT

Figure 3. Marginal error in measuring f_{NL}, against the surveyed area for different configurations, with fixed MeerKAT observing time of 4000 h. Left-hand panel: MeerKAT with *L* band (dashed, blue) and *UHF* band (dot–dashed, red). Right-hand panel: DES on its own (solid, green); multitracer MeerKAT *L* band × DES (dashed, blue); multitracer MeerKAT *UHF* band × DES (dot–dashed, red).

Table 1. Marginal errors on f_{NL} for H I intensity map surveys with MeerKAT *L*- and *UHF* bands, a DES photometric survey, multitracer analyses combining DES and each MeerKAT band. (We assume 5000 deg² survey area, and 4000 h MeerKAT time.)

	$\sigma(f_{NL})$
MeerKAT *L* Band	56.5
MeerKAT *UHF* Band	43.8
DES	11.9
MT: MeerKAT *L* Band × DES	3.6
MT: MeerKAT *UHF* Band × DES	2.3

5 CONCLUSIONS

Table 1 summarizes the marginal errors on f_{NL} for the individual and multitracer cases, using a survey area of 5000 deg² and MeerKAT's integration time of 4000 h. DES with the MeerKAT *L* band is two times better than *Planck*, while DES combined with the *UHF* band improves on *Planck* by a factor of 3. In both cases, the multitracer is forecast to beat *Planck* on f_{NL} within the next few years.

The right-hand panel of Fig. 3 also shows that the multitracer technique is powerful enough to improve the forecast error on f_{NL} even with a smaller surveyed area, as can be seen by comparing

DES on its own to the multitracer of DES with MeerKAT. This can be contrasted with single-tracer measurements, which require larger volumes to reduce the error bars.

Fig. 4 shows how our results vary with integration time and surveyed area. Contours are plotted for $\sigma(f_{NL})$ when both the overlap survey area and the MeerKAT integration time are varied. Even a survey overlap area of $\gtrsim 2000\,\text{deg}^2$ and a MeerKAT observation time $\gtrsim 2000\,\text{h}$ suffices to give an improvement over *Planck*-level accuracy with the *UHF* band × DES (right-hand panel). The same area and integration time with the *L* band × DES (left-hand panel) gives an improvement on full DES (with 5000 deg²).

We have assumed that all multipoles down to $\ell = 3$ can be used when considering a 5000 deg² survey. If the largest scales are not accessible, the result worsens as we can see in Fig. 5 (left-hand panel). The effect is more prominent for the single tracer case, as shown for DES. In the multitracer case, the accuracy is only mildly degraded.

We chose to truncate the sum in the Fisher matrix at $\ell = 300$, even when higher ℓ would still correspond to linear scales. Although this choice may seem arbitrary, we can see in Fig. 5 (right-hand panel) that not much more information is added for $\ell \gtrsim 150$.

We use models for the H I and galaxy bias to provide the fiducial values in each redshift bin. The uncertainties in bias modelling can be mitigated by marginalizing over the bias in each redshift bin. The results of Alonso & Ferreira (2015); Fonseca et al. (2015) indicate that uncertainties in the bias are less important than those in the magnification bias and evolution bias. We also incorporate
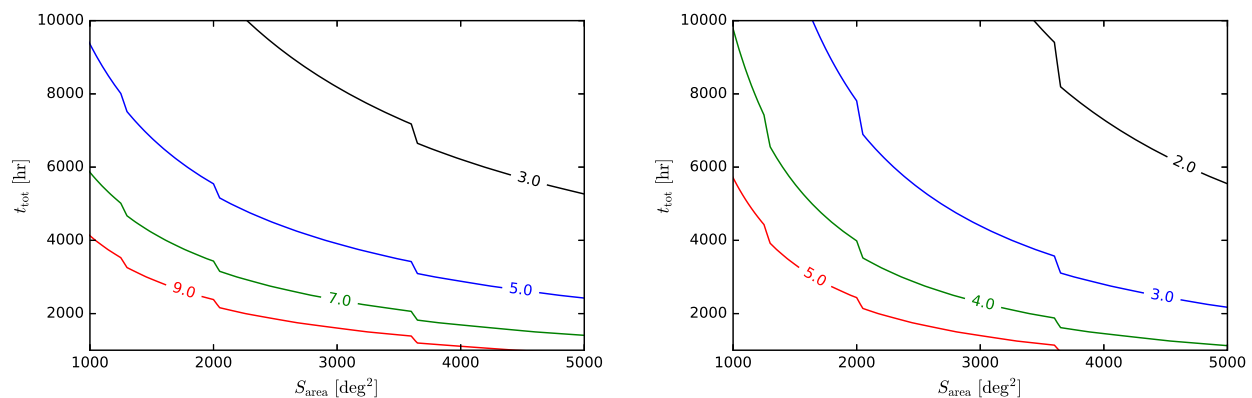

Figure 4. Contour plot of $\sigma(f_{NL})$ against survey area and observing time, using the multitracer with MeerKAT and DES. Left-hand panel: *L* band × DES. Right-hand panel: *UHF* band × DES.
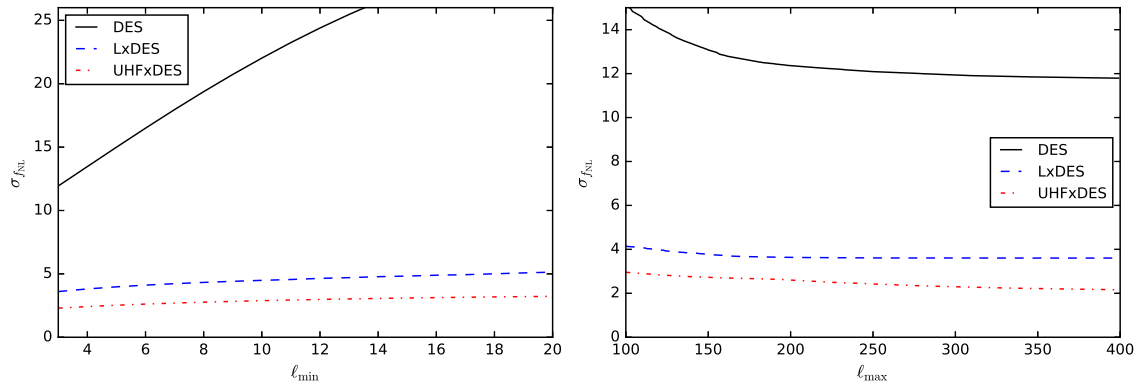
Figure 5. $\sigma(f_{NL})$ as a function of the minimum multipole (left-hand panel) and maximum multipole (right-hand panel) used in the Fisher forecast (with 5000 deg^2 survey area and 4000 h MeerKAT time).

uncertainties in these by marginalizing over the parameters ε_{WL} and ε_{GR}, respectively.

We do not include foregrounds and observational systematics in creating the maps in the full covariance matrix – but the multitracer technique includes cross-correlations and thereby lessens the impact of individual systematics and of foreground residuals.

We conclude that the best contemporary radio and optical surveys, i.e. MeerKAT and DES, when combined via the multitracer technique, can improve on the *Planck* error bars for f_{NL}, well before the next-generation surveys deliver data. This is important not only for improving on *Planck* – but also because it can serve as a 'proof of concept' for the multitracer technique applied to primordial non-Gaussianity. The MeerKAT–DES multitracer will effectively be a pathfinder for radio–optical multitracing with next-generation surveys, such as SKA–LSST or SKA–*Euclid*.

REFERENCES

Abramo L. R., Leonard K. E., 2013, MNRAS, 432, 318
Alonso D., Ferreira P. G., 2015, Phys. Rev. D, 92, 063525
Alonso D., Bull P., Ferreira P. G., Maartens R., Santos M., 2015, ApJ, 814, 145
Bonnett C. et al., 2016, Phys. Rev. D, 94, 042005
Bonvin C., Durrer R., 2011, Phys. Rev. D, 84, 063505
Bruni M., Crittenden R., Koyama K., Maartens R., Pitrou C., Wands D., 2012, Phys. Rev. D, 85, 041301
Bull P., 2016, ApJ, 817, 26
Camera S., Santos M. G., Maartens R., 2015a, MNRAS, 448, 1035
Camera S., Maartens R., Santos M. G., 2015b, MNRAS, 451, L80
Challinor A., Lewis A., 2011, Phys. Rev. D, 84, 043516
Clerkin L., Kirk D., Lahav O., Abdalla F. B., Gaztanaga E., 2015, MNRAS, 448, 1389
Dalal N., Dore O., Huterer D., Shirokov A., 2008, Phys. Rev. D, 77, 123514
Di Dio E., Montanari F., Lesgourgues J., Durrer R., 2013, J. Cosmol. Astropart. Phys., 1311, 044
Ferramacho L. D., Santos M. G., Jarvis M. J., Camera S., 2014, MNRAS, 442, 2511
Fonseca J., Camera S., Santos M. G., Maartens R., 2015, ApJ, 812, L22
Gabasch A. et al., 2006, A&A, 448, 101
Gong Y., Chen X., Silva M., Cooray A., Santos M. G., 2011, ApJ, 740, L20
Hall A., Bonvin C., Challinor A., 2013, Phys. Rev. D, 87, 064026
Hamaus N., Seljak U., Desjacques V., Smith R. E., Baldauf T., 2010, Phys. Rev. D, 82, 043515
Hamaus N., Seljak U., Desjacques V., 2011, Phys. Rev. D, 84, 083509
Jeong D., Schmidt F., Hirata C. M., 2012, Phys. Rev. D, 85, 023504
Ma Z.-M., Hu W., Huterer D., 2005, ApJ, 636, 21
Matarrese S., Verde L., 2008, ApJ, 677, L77
McDonald P., Seljak U., 2009, J. Cosmol. Astropart. Phys., 0910, 007
Planck Collaboration XVII, 2015, A&A, 594, 17
Pourtsidou A., Bacon D., Crittenden R., Metcalf R. B., 2016a, MNRAS, 459, 863
Pourtsidou A., Bacon D., Crittenden R., 2016b, preprint (arXiv:1610.04189)
Raccanelli A., Montanari F., Bertacca D., Doré O., Durrer R., 2016, J. Cosmol. Astropart. Phys., 1605, 009
Santos M. et al., 2015, Proc. Sci., Cosmology from a SKA HI intensity mapping survey. SISSA, Trieste, PoS(AASKA14)019
Seljak U., 2009, Phys. Rev. Lett., 102, 021302
Smith R. et al., 2003, MNRAS, 341, 1311
Tegmark M., Taylor A., Heavens A., 1997, ApJ, 480, 22
Weinberg D. H., Dave R., Katz N., Hernquist L., 2004, ApJ, 601, 1
Yamauchi D., Takahashi K., Oguri M., 2014, Phys. Rev. D, 90, 083520
Yoo J., 2010, Phys. Rev. D, 82, 083508
Yoo J., Hamaus N., Seljak U., Zaldarriaga M., 2012, Phys. Rev. D, 86, 063514

This paper has been typeset from a TeX/LaTeX file prepared by the author.